

Fabrication and curing conditions effects on the fatigue behavior of a structural adhesive

Andrea I. M. Foletti^a, José Sena Cruz^b, Anastasios P. Vassilopoulos^{a1}

^a Composite Construction Laboratory (CCLab), Ecole Polytechnique Fédérale de Lausanne (EPFL),
1015 Lausanne, Switzerland

^b ISE/IB-S, Department of Civil Engineering, University of Minho, 4800-058, Guimarães, Portugal

Abstract:

This paper investigates the effects of degassing, curing and post-curing conditions on the tensile quasi-static and fatigue behavior of a cold-curing structural epoxy adhesive. Quasi-static experiments performed at standardized and high displacement rates similar to those imposed to the material under fatigue loading, in order to derive comparable results from both loadings, and tensile-tensile fatigue tests at a fixed stress ratio, were carried out. Digital image correlation, video extensometer, thermal camera, digital camera and microscope were used to record the evolution of the strain and temperature, and assess the damage evolution during and after loading. The results shown that degassing can improve the material behavior when curing at ambient temperatures, since it assist the removal of several small voids from the bulk adhesive. However, when curing the material at high temperatures, immediately after mixing, the degassing does not offer any advantage, and the material's long-term performance decreases.

Keywords: Fatigue, composites, adhesives, curing, degassing

1. Introduction

In civil engineering, adhesives have been used for more than 50 years [1, 2] for connecting structural elements without harming their structural integrity by drilling. The use of adhesives, initially, has been limited for strengthening, maintenance, or secondary connections [3] as was evidenced by the development of several retrofitting reinforcement methods [4, 5]. Nevertheless, recently structural adhesives have been used in critical bonding of structures, notably in bridge engineering and the wind energy, as they offer advantages against other joining methods [6, 7]. Applications in bridge and wind-turbine engineering present large and thick bond-lines which undergo important fatigue loadings during their lifetime [8-10].

Cold-curing structural adhesives can be used on site for connections of e.g. prefabricated bridge decks to girders reducing the traffic disruption time as was proved in [6]. In such cases however, the evolution of the curing degree of the cold-curing adhesive is of crucial importance as it will determine when the structure will be available for operation. The adhesive curing depends on the ambient temperature at which the reaction will occur, and the adhesive durability will be affected by the curing conditions [11-13]. Heating the adhesive during the polymerization can assist the curing. Investigation of the effect of curing temperature on the curing degree of Sikadur 330 was performed in [14], showing that higher curing temperatures reaching 90 °C affected significantly the curing degree of the examined epoxy resin. Specimens cured for two weeks at ambient temperatures could reach curing degree of around 94%, while the curing degree could be increased, reaching ca. 99% with 30 minutes of post-curing at 90°C. Above this temperature, and especially when exceeding ca. 100°C there is a risk to damage the material. It has been shown in several studies see e.g. [15-17] that post-curing accelerates the development of the physical, e.g., the glass transition temperature, and the mechanical properties, e.g., the tensile strength and the Young's modulus. As shown in [14] the glass transition temperature, and

¹ Corresponding Author's contact details: e-mail: anastasios.vassilopoulos@epfl.ch, Tel: +41216936393.

the strength and stiffness of the investigated cold-curing structural adhesive, are functions of the curing degree. Post-curing of materials approaching, but not achieved fully cure, can lead to significant increase of the glass transition temperature and the mechanical properties [14, 15, 18]. The increase of the properties is correlated to the increase of the cross-linking, [19-21]. Nevertheless, despite the faster evolution of the properties, the accelerated curing by heating does not always lead to improved properties, since it can cause porosity leading to a less favorable stress distribution as shown in [22].

During the mixing of the adhesive components, air voids can be entrapped in the material volume. If not removed, e.g., by a degassing process, these gas bubbles remain in the material after the curing, form initial imperfections and become potential risk locations. Several researches have been carried out on this topic investigating the effect of hot curing and post curing conditions on the adhesives porosity, e.g. [22-24]. When heated, the entrapped gas dilates resulting in a higher porosity [24], affecting the mechanical properties of the adhesive. Degassing during or after mixing of the adhesive components [22] was shown to increase the nominal strength, nevertheless, accelerated curing at high temperatures led to lower strength and stiffness compared to specimens of the same age cured at room temperature. This property reduction was assigned to the porosity caused by the accelerated curing process. Strength, stiffness, Poisson ratio, and strain at failure of polymer materials are also dependent on the loading rate [25-27]. This evolution of the properties has been linked to the relaxation state of the atoms. At higher strain rate, the atoms are less relaxed and therefore, they necessitate more fracture energy for the final fracture of the sample resulting in higher strength [28].

Literature review showed that studies on the effect of preparation and curing conditions on the behavior of epoxy structural polymers focused on the quasi-static properties of the material. Works on the fatigue behavior of structural adhesives were mostly limited to joint configurations [29-34] while fewer works have been carried out on bulk adhesive specimens, e.g. [35-43]. Nevertheless, as mentioned above, in contrast to aerospace, joints in civil engineering and in wind energy have thick bond-lines, of several millimeters and usually undergo multiaxial loading conditions [6, 9]. In such cases, the study of the bulk material properties is necessary. Since certain properties, such as the (fatigue) tensile strength, stiffness, strain at failure, and Poisson ratio can hardly be estimated by joint experiments, investigations of the bulk specimen performance are indispensable when such material data should be implemented in numerical/analytical modelling [44].

Simple phenomenological modeling based on S-N equations [45], widely used in modeling the fatigue behavior of composite laminates [46], seems to appropriately simulate the fatigue behavior of epoxy adhesives, e.g. [35, 37, 40-42]. The S-N curves of epoxy resins tend to have similar slopes of glass fiber epoxy laminates, when the fatigue failure of the latter is matrix dominated, e.g., [47, 48]. This shows that the fatigue damage propagation in laminated composites is controlled by the matrix, and that degradation of the laminae under fatigue loading first occurs in the matrix, while damage in the fibers is the result of the matrix degradation. According to [49] the limiting factor in fatigue is not the fiber but the interface or the matrix itself, as also discussed in [50, 51]. During fatigue loading the material stiffness changes. For composite laminates, fatigue stiffness, usually drops with loading because of damage induced to the material volume [46]. Nevertheless, in several cases stiffness increase was recorded, due to fiber realignment in off-axis laminates [52]. Such measurements for bulk epoxy adhesives are rare in the literature, e.g., [35, 38] and stiffness increase at the early stages of fatigue loading have been reported [35], although this phenomenon was not sufficiently explained.

Epoxy adhesives are sensitive to hysteretic heating [43]. Nevertheless, previous studies, e.g. [35] showed that the frequencies up to 10-15 Hz do not affect the fatigue behavior. In general, if the frequency is sufficiently low, and the specimen is thin, the energy resulting from self-heating can be released to the environment without affecting the integrity of the bulk material. Nevertheless, the rate effect must be considered when it is intended to mix quasi-static strength and fatigue data in the modeling. In that case, quasi-static data derived at rates similar to those achieved during fatigue loading (usually much higher than the standardized rates for quasi-static experiments) must be used.

Only few studies performed for the investigation of the effect of curing conditions on the fatigue behavior of bulk adhesives and to the authors' knowledge, there is no investigation on the influence of

the preparation method and the curing conditions on the fatigue performance of bulk epoxy structural adhesives. Therefore, this paper presented the results of the investigation of the preparation and curing conditions influence on the fatigue behavior of a commercial cold-curing structural adhesive. An extended experimental campaign was carried out including quasi-static and fatigue experiments for four types of specimen, each one prepared under different conditions. Standardized, and similar to those imposed to the material under fatigue loading, displacement rates, were applied during the quasi-static experimental campaign. The influence of the preparation method and the effect of the curing process are discussed through the phenomenological analysis of the material behavior and a fractographic analysis of the specimens' failure surfaces.

2. Material, experimental program and test methods

2.1. Material and sample definition

The epoxy adhesive, Sikadur-330 by Sika Schweiz AG, was used in this study. The primary commercial use of this cold-curing adhesive or resin is manual application to surfaces in order to bond FRP strips and impregnate FRP fabrics employed to strengthen existing concrete or steel structures. Sikadur-330 is a thixotropic bi-component adhesive comprising a bisphenol-A-based epoxy base resin and a hardener consisting of aliphatic amines. The mixing ratio is 4:1 (A:B). It contains a small quantity of silica-based fillers (less than 20%) [14]. According to the technical data sheet [20] and research performed at CCLab/EPFL [14, 21, 35], the tensile strength after 7 days of curing at 23°C reaches around 30 MPa and the elastic modulus around 4.5 GPa, with a glass temperature of approximately 44°C.

The dumbbell-shaped geometry, recommended by ASTM D638-14 [53] ("Type 1 specimen"), was adopted for the quasi-static tensile tests, as well as the tensile-tensile fatigue tests carried out in the scope of the present work (see Fig. 1).

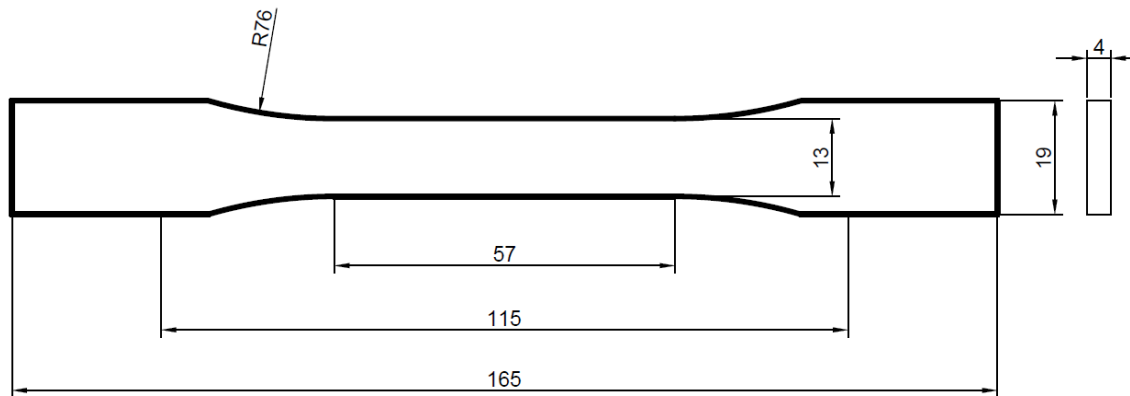


Figure 1. ASTM D638-14 - type 1 "Dumbbell" specimen [mm]

2.2. Specimen's preparation

Four different series of specimens were prepared in order to study (i) the influence of the temperature during curing and post-curing phases and (ii) the influence of the degassing during the mixing phase, on the tensile quasi-static and fatigue behavior of the epoxy adhesive. Aluminum molds were used to fabricate the specimens. To facilitate the demolding, Teflon sheet was used on the bottom surface of the molds and release agent was placed on their lateral faces. The two adhesive components were mixed for all specimen series at laboratory conditions, temperature $T=21\pm3^{\circ}\text{C}$ and relative humidity $RH=40\pm10\%$. After mixing the two adhesive components, the homogenized compound was poured in the mold with the help of a spatula. Special care to fill completely the mold and avoiding the introduction of air was taken. After the casting, the specimens were left for 7 days in a climatic chamber

(CC) with fixed temperature and relative humidity ($T=20^{\circ}\text{C}$ & $\text{RH}=60\%$). An oven was used for post-curing the specimens at 90°C for 30 min. After this period, the oven was turned-off and the doors were opened in order to allow a smooth cool down.

The first series of specimens (**Ref**) was used as reference. After casting at $21\pm 3^{\circ}\text{C}$, $40\pm 10\%$, the **Ref** specimens were placed in the CC for seven days and afterwards were tested within the next three days. The second set of specimens (**R20**) was prepared in the same way as the **Ref** specimens, however, after seven days of curing in the CC, they were submitted to a post-curing at 90°C for 30 min.

For the last two sets (**V20** and **V90**), a degassing procedure was followed. After mixing the adhesive components the compound was put in a vacuum pump (1 bar pressure) for 9 min (a process of three consecutive cycles of 3 min each). After casting, the **V20** specimens were left in the CC for seven days, prior the post-curing at 90°C for 30 min, as in the case of **R20** series. The **V90** specimens subjected to a post-curing at 90°C for 30 min, immediately after casting.

Specimens of series **R20**, **V20** and **V90** were tested within one month after completion of the designated curing cycles. A summary of the preparation and curing conditions is given in Table 1.

Table 1. Preparation and curing conditions of different specimen series

Series	Degassing	Curing in CC (20°C , 60%)	Post-curing at elevate temperature (90°C , 30 min)
Ref	No	7 days	No
R20	No	7 days	Yes, after 7 days
V20	Yes	7 days	Yes, after 7 days
V90	Yes	No	Yes, after casting

2.3. Dynamic Mechanical Analysis

Dynamic mechanical analysis (DMA) was carried out to measure the glass transition temperature (T_g) and estimate the curing degree of each specimen type by performing a second DMA scan. DMA experiments were performed using a TA Instruments DSC Q800 system under constant displacement of $15\text{ }\mu\text{m}$ at a frequency of 1 Hz using a single-cantilever configuration. The specimen geometry was $35\times 10\times 3\text{ [mm]}$. A heating rate of $2^{\circ}\text{C}/\text{min}$ was selected to run DMA scans between -20°C and $+120^{\circ}\text{C}$, with a 10 min isothermal period in both extreme temperature values, according to ASTM D7028-07 [54], designating that the limits should be at least 50°C below and above the expected T_g of the material, without damaging the specimen. The glass transition temperature was defined as the onset value of the storage modulus decay. It was obtained from the intersection of the two tangent lines of the storage modulus curve: one tangent to the upper plateau and the other tangent to the linear decreasing segment at the glass transition region. Table 2 shows the obtained values.

Table 2. Glass transition temperature from DMA

Set	$T_g\text{ [}^{\circ}\text{C]}$
Ref	49.6 ± 1.1
R20	58.6 ± 0.2
V20	60.7 ± 3.1
V90	61.7 ± 0.7

The glass transition temperature for the **Ref** specimen is in the range of previous work [14, 35] and the value for the post-cured specimens are all in the range of the glass transition temperature given by the technical data sheet (58°C), which is the value for thirty days of curing at $+30^{\circ}$.

2.4. Quasi-static and high-rate experiments

The quasi-static tensile experiments were performed according to ASTM D638-14 [53], using an MTS 810 Landmark servo-hydraulic loading machine, calibrated at a load capacity of 5 kN with $\pm 0.5\%$ of applied force accuracy (Fig. 2). All the experiments were carried under ambient laboratory conditions

($T=22\pm3^{\circ}\text{C}$, $\text{RH}=40\pm10\%$). A constant displacement rate of 5 mm/min was adopted for testing the specimens, according to ASTM D638-14. Additional tensile experiments were performed at the displacement rates of 160, 240 and 550 mm/min in order to investigate the rate effect on the material performance and to obtain strength values at rates similar to those used in fatigue loading. This procedure allows the comparison of the results obtained from quasi-static and fatigue loadings. All the monotonic tensile experiments are referred as "quasi-static" in the rest of the document.

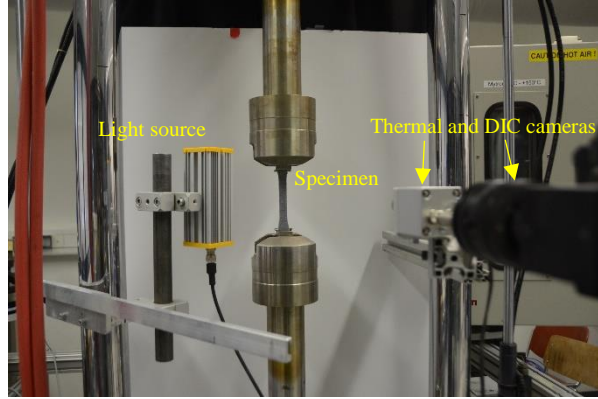


Figure 2. Testing rig and instrumentation

The axial strains were estimated by the displacements measured by the linear variable differential transducer (LVDT) of the actuator and a video extensometer (VE) with a gage length of 50 mm. A digital image correlation (DIC) system was also used for obtaining the full field surface strain measurement, and the Poisson ratio, as well as to identify the damage progression throughout the experiments. For both VE and DIC, a Point Grey – Grasshopper3 camera with a resolution of 2.2 Megapixels and a Fujinon HF35SA-1 35mm F/1.4 lens, with a data acquisition frequency up to 162 Hz was used.

The nominal strength was estimated as the ratio of the maximum load over the cross sectional area, while the tensile elastic modulus (stiffness) was defined by a liner interpolation to the slope of the stress-strain curve between 0.05% and 0.25% of strain. Specimens that presented tab failure were not considered in the analysis.

The specimens were labelled according to the series and the displacement rate, followed by a serial number indicating the specimen number per displacement rate. For example, the specimen R20_005_01 is the first **R20** specimen loaded at 5 mm/min.

2.5. Fatigue experiments

The fatigue experiments were performed at the same machine and under the same environmental conditions as the quasi-static experiments, following the ASTM D7791-12 [55]. Experiments were performed under load control with a stress ratio $R=\sigma_{\min}/\sigma_{\max}=0.1$ and a sinusoidal loading waveform. Nominal cyclic stress was calculated by dividing the applied cyclic loads by the average cross sectional area of each specimen. The tension-tension loading profile was chosen to avoid buckling and to be comparable with other fatigue surveys, mainly tested with the same R ratio. In order to avoid unwanted slippage at the clamping region during the experiments, and to reduce the amount of tab failures, $25\times20\times2$ [mm] aluminum tabs were glued with cyanoacrylate glue to the extremity of the specimens.

A range of load (stress) levels was selected for each S-N curve aiming to collect data for lifetimes ranging between 10 and 2×10^6 cycles. Specimens exceeding 2×10^6 cycles were considered as run-outs and were subjected to residual strength tests after the interruption of the loading at arbitrary numbers of cycles. An adequate number of specimens was examined for each S-N curve to comply with the requirements of ASTM E739-10 [56] regarding the appropriate number of specimens that must be examined in order to assure that a random sample of the material is being tested and to obtain S-N curves with statistical significance.

In order to avoid influence of different displacement rates throughout the campaign, the loading frequency was adapted per stress level in order to keep a constant loading rate (\dot{F}) for all experiments, as was done also in other works, e.g., [48, 52]. The frequency, f , of each load level at the cyclic load amplitude, F_a , was calculated by solving the following equation:

$$\dot{F} = 4F_a f \quad (1)$$

Previous works of the authors group on the same structural adhesive [35], showed that frequencies up to 15 Hz did not cause any significant hysteretic heating. In this work, this frequency was selected for the high cycle fatigue region, and all other frequencies for higher stress levels were estimated based on Eq. (1). Details regarding the fatigue experiments are given in the experimental results section. The surface temperature was continuously monitored by using an infrared-thermal camera (thermoIMAGER TIM), with 0.1°C resolution to validate the selected parameters.

Loading for the fatigue experiments was applied on the specimens by a ramp up to the mean value of the cyclic load at a rate of 50 N/s, followed by a sinusoidal spectrum of fatigue cycles at the given load amplitude and frequency until failure.

The displacements measured by the LVDT actuator, the load and the number of cycles were recorded through the fatigue cyclic loading of all the specimens. In addition, the same video camera as in the quasi-static tests was used as VE and for DIC recording. A comparison of the strains obtained from the video extensometer and the ones derived from LVDT readings have shown no significant differences, since no slippage at the clamping zone has occurred, and therefore, the LVDT data has been used in this work.

The specimens were labelled according to the series and the maximum applied cyclic load, followed by a serial number indicating the specimen number per load level. For example, the specimen Ref_1550_02 is the second **Ref** specimen loaded at 1550 N maximum load.

2.6. Fracture surface investigation

In order to examine the fracture of the specimens, post mortem photos of the fracture surfaces were taken using the digital handheld microscope Dino-Lite AD7013MZT. This microscope is equipped with a 5-megapixel sensor and can provide up to 240× magnification and a resolution of 2592×1944 pixels. Specimens failed after quasi-static and fatigue experiments were inspected.

3. Results and discussion

3.1. Quasi-static and high displacement rate

Specimens from the four different series have been tested at various displacement rates. The 5 mm/min rate was chosen according to ASTM D638-14 [53] as the reference rate that leads to a failure in 0.5 to 5 min. As mentioned above, the higher rates were chosen to approach those used in the fatigue experiments. Table 3 summarizes all the quasi-static experimental results. The values are consistent with those derived from previous quasi-static experiments on the same adhesive [14, 21, 35]. The stiffness at 5mm/min for all specimen series was by approximately 10-15% lower than the 4.5 GPa given in the data sheet [20], probably due to the 20°C temperature in the CC, which is lower than the 23 °C used in the data sheet. In contrast to stiffness, the tensile strength is higher than the value given in the data sheet (30 MPa).

A comparison of the results shows that stiffness increases for every series with increasing displacement rate. The stiffness is lower for **Ref** specimens, as was expected since they were not post-cured, higher for **R20** and **V20** specimens, while the highest values are estimated for the **V90** specimen series. The effect of the post-curing and the degassing on the strength of the material is more evident at low displacement rates where all post-cured series specimens attained at least 11% higher strength. At the highest loading rate (550 mm/min) specimens from all series have the same behavior with same stiffness, strength and strain to failure.

This evolution of properties was linked to the relaxation state of the atoms in [28]. At higher strain rates, the atoms are less relaxed hence, they necessitate more fracture energy for the final fracture of the sample resulting in higher strength. The strain at failure decreases (more pronounced for the degassed series) with the increase of displacement rate, due to the stiffening of the specimens with the displacement rate.

Table 3: Quasi-static experimental results

Series	Displacement rate [mm/min]	Number of specimens	Stiffness [MPa]	Strength [MPa]	Failure strain (%)
Ref	5	6	3992 (2.3%)	33.3 (7.8%)	1.07 (13.75%)
R20	5	8	3866 (2.6%)	36.9 (13.1%)	1.18 (19.94%)
V20	5	6	3991 (2.2%)	41.2 (12.6%)	1.31 (19.12%)
V90	5	5	4210 (3.0%)	39.5 (10.1%)	1.13 (12.87%)
Ref	240	--	--	--	--
R20	240	3	4081 (2.6%)	42.0 (8.2%)	1.25 (14.45%)
V20	240	1	4179 (--)	37.9 (--)	1.06 (--)
V90	240	2	4613 (--)	41.4 (--)	1.03 (--)
Ref	360	--	--	--	--
R20	360	3	4082 (1.2%)	39.8 (10.6%)	1.12 (12.45%)
V20	360	--	--	--	--
V90	360	2	4646 (--)	44.4 (--)	1.15 (--)
Ref	550	7	4472 (3.0%)	40.1 (11.4%)	1.06 (16.88%)
R20	550	6	4234 (2.9%)	41.6 (8.2%)	1.16 (12.52%)
V20	550	5	4328 (3.9%)	41.8 (11.3%)	1.14 (16.57%)
V90	550	5	4493 (2.0%)	39.7 (13.5%)	1.04 (14.24%)

Note: the values between parentheses are the corresponding coefficients of variation (COV).

An increasing trend was noticed for both stiffness and strength of all specimens with increasing displacement rate as shown for a typical example in Fig. 3, for the **R20** series. Higher displacement rates increase the mechanical properties, and especially the stiffness, affecting consequently the strain to failure as the material becomes stiffer. The strength shows an increasing trend with displacement rate, however, less obvious due to the brittle failure of the material. Despite the scatter, results of series **R20** in Table 3 show a clear increase of the mechanical properties from 5 mm/min to 240 mm/min and almost steady-state behavior after this displacement rate. In fact, 5 mm/min to 240 mm/min corresponds to an increase of the speed rate of 4700%, while of the other cases is approximately equal to 50%. For series **Ref** and **V20** similar trend can be observed. However, for the case of the **V90** series specimens, the mechanical properties were not significantly affected by the displacement rate. This can be attributed to the immediate curing at high temperature adopted in this series.

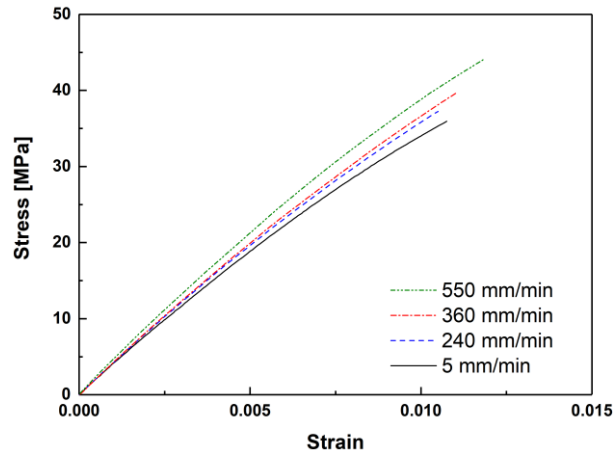


Figure 3. Effect of displacement rate on mechanical properties (specimens R20_005_03, R20_240_03, R20_360_02, R20_550_05)

A comparison of the stiffness and strength increase with increasing displacement rate for the different specimen series is presented in Fig. 4, showing that the **Ref** specimens exhibited more significant changes in both strength and stiffness when loaded in higher displacement rates. This figure also shows that stiffness depends on the displacement rate, while strength, especially for the degassed specimen series seems to be independent of it. The scatter in strength is much higher than that in stiffness (the maximum COV for stiffness and strength was 3.9% and 13.5%, respectively), as expected since strength is sensitive to the local microstructure of each specimen and affected severely by defects.

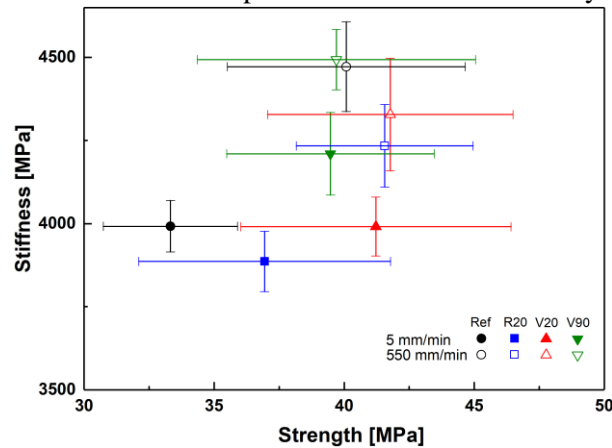


Figure 4. E-modulus and strength under different displacement rates

DIC strain measurements allow the estimation of the Poisson ratio. Results presented in Table 4 indicate that the Poisson ratio is not sensitive to the displacement rate, being around the value of 0.32, in the expected range for such epoxy systems, e.g. [14]. The degassing seems to cause a slight, although insignificant, increase of Poisson ratio.

Table 4: Poisson ratio

Specimen series	Displacement rate [mm/min]	Poisson ratio	
		Mean value [-]	COV (%)
Ref	5	0.301	--
	550	0.293	12.1
R20	5	0.325	3.1
	550	0.317	6.8
V20	5	0.330	--
	550	0.332	2.7
V90	5	0.311	--

	550	0.360	3.7
--	-----	-------	-----

Typical failure surfaces from failed specimens from all series after quasi-static loading at low and high displacement rates are presented in Fig. 5-6, showing that the degassing process reduces the quantity of air bubbles inside the resin. Most of the smaller voids, presented in both **Ref** and **R20** series are not existent in the degassed series (see Fig. 5). Bigger voids appear in all specimen types, probably due to the manual pouring and casting of the specimens, although their presence does not seem to affect the material strength. It is supposed that the regular ellipsoidal shape of such big voids does not create any stress concentrations in the material volume. Nevertheless, the smaller voids do affect the strength of the specimens and their presence in the non-degassed series could explain their lower strength.

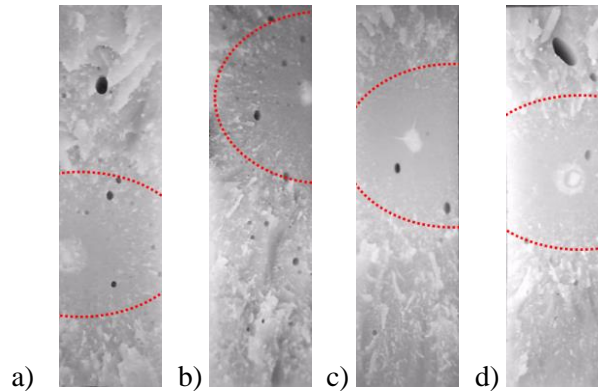


Figure 5 Fracture surface of specimens at 5mm/min; a) Ref_005_02, b) R20_005_05, c) V20_005_02, d) V90_005_01 – Scale: entire specimen cross section (4×13 mm²)

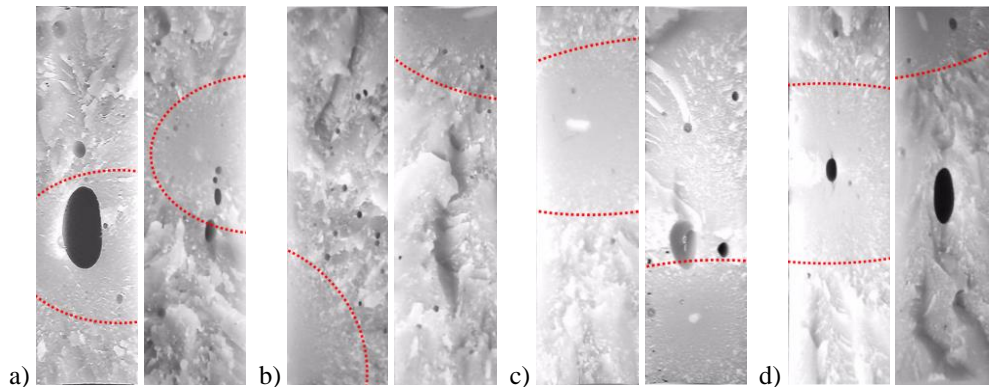


Figure 6: Effect of displacement rate on the fracture surface; a) Ref_005_04, Ref_550_10, b) R20_005_06, R20_550_19 c) V20_005_05, V20_550_12 d) V90_005_03, V90_550_13 – Scale: entire specimen cross section (4×13 mm²)

The majority of the fracture photos show two zones, “zone I”, a “cleaner” zone centered around the location where, supposedly, the fracture initiates (see e.g., the areas inside the red ellipse in Fig. 5d, or Fig. 6c)) and “zone II”, a bare zone where the material is brutally torn apart (see e.g., Fig. 5b, outside the red ellipse, and Fig. 6a, outside the red ellipse as well). Fig. 6 shows that zone II is more pronounced when the speed of testing is higher. The formation of these two zones is related to the brittle behavior of the Sikadur 330 epoxy system. After crack initiation, the crack area increases in zone I, and when a critical area is reached the specimen fails abruptly often resulting in the breaking of a part of the specimen as illustrated in the photo taken by the high-speed camera used for the DIC measurements in Fig 7.

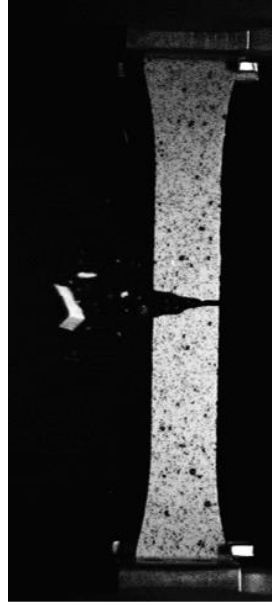


Figure 7. Photo taken at the moment of failure of specimen R20_005_03

3.2. Fatigue

3.2.1 Temperature measurements

During fatigue, loading the temperature of the specimens increased due to the self-generated heating because of internal friction. Fig. 8a shows the typical evolution of the ambient, the average and the maximum surface temperature during the fatigue life of a reference specimen tested at ~14 Hz. The surface temperature, both average and maximum, does not increase considerably during fatigue loading, being in most of the cases a couple of degrees above the ambient temperature, as was also reported in [35]. The specimen surface temperature for this one, but also for all other specimens increased rapidly at the beginning of the experiments, and rest almost stable for the remaining cycles until failure. Maximum temperatures well below 30 °C were measured in all cases, remained below the glass transition temperature of the material, see Table 2. Actually, the specimen temperature was more affected by the changes of the ambient temperature than the hysteretic heating due to the fatigue loading, as shown in Fig. 8b.

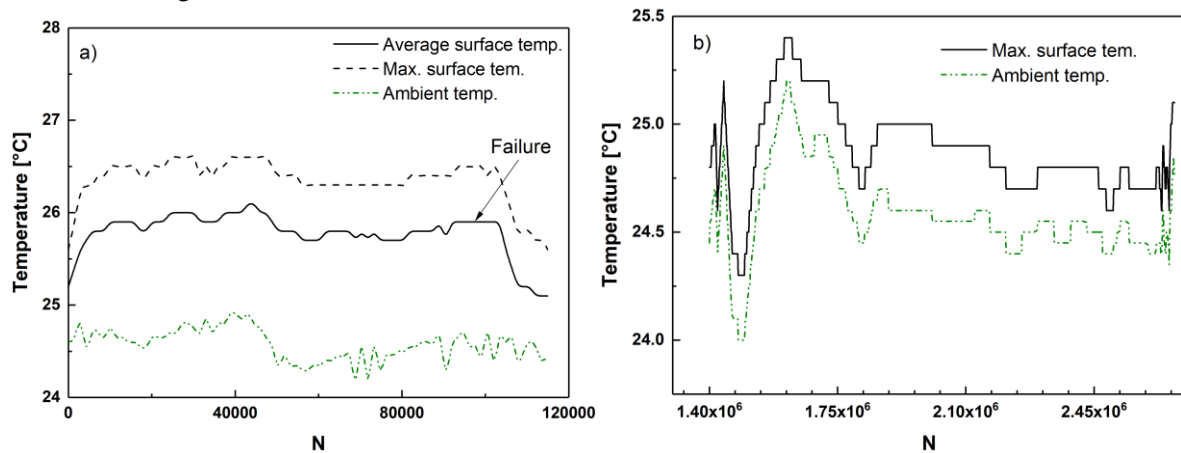


Figure 8. Temperature evolution a) Ref_785_01 b) Ref_635_02

3.2.2 Fatigue behavior

Tables 5-8 summarize the fatigue results for all specimens, with run-out specimens shown in bold. As mentioned above, the fatigue experiments exceeding 2×10^6 cycles were interrupted at random numbers of cycles and subjected to a residual strength test at 5 mm/min. Results of this experimental investigation

are summarized in Table 9. Results from tab failures or specimen failures during the first cycle were excluded.

Table 5. Fatigue results for the **Ref** specimens

Specimen ID	Max. cyclic load [N]	Max. cyclic stress [MPa]	Frequency [Hz]	Cycles to failure
Ref_1640_01	1640	34.36	6	88
Ref_1550_01	1550	31.03	6.5	57
Ref_1550_02	1550	30.68	6.5	434
Ref_1550_03	1550	30.64	6.5	46
Ref_1450_01	1450	28.85	7	310
Ref_1450_02	1450	28.68	7	274
Ref_1450_03	1450	28.22	7	93
Ref_1275_01	1275	25.75	8	727
Ref_1275_02	1275	25.43	8	679
Ref_1275_03	1275	24.80	8	1440
Ref_1090_01	1090	21.91	9.2	2314
Ref_1090_02	1090	21.44	9.2	862
Ref_1090_03	1090	21.32	9.2	1259
Ref_1090_04	1090	21.14	9.2	4911
Ref_910_01	910	18.15	11	9607
Ref_910_02	910	17.67	11	14016
Ref_820_01	820	16.73	13	18354
Ref_785_01	785	16.00	13.9	100576
Ref_745_01	745	15.00	10	579654
Ref_730_01	730	14.85	15	902406
Ref_730_02	730	14.71	15	182860
Ref_730_03	730	14.06	15	20859
Ref_730_04	730	14.06	15	28810
Ref_720_01	720	14.50	10	96629
Ref_720_02	720	14.50	10	152836
Ref_635_01	635	12.50	15	129467
Ref_635_02	635	12.45	15	2669910

Table 6. Fatigue results for the **R20** specimens

Specimen ID	Max. cyclic load [N]	Max. cyclic stress [MPa]	Frequency [Hz]	Cycles to failure
R20_1800_01	1800	34.97	5.5	33
R20_1800_02	1800	34.94	5.5	242
R20_1800_03	1800	34.92	5.5	156
R20_1550_01	1550	31.20	6.5	1819
R20_1550_02	1550	30.98	6.5	1089
R20_1450_01	1450	29.22	7	586
R20_1450_02	1450	28.88	7	1067
R20_1275_01	1275	25.64	8	602
R20_1275_02	1275	25.34	8	891
R20_1275_03	1275	25.11	8	5926
R20_1275_04	1275	24.96	8	1421
R20_1275_05	1275	24.76	8	8701
R20_1090_01	1090	21.72	9.2	8727
R20_1090_02	1090	21.50	9.2	4702
R20_1090_03	1090	20.82	9.2	11497
R20_910_01	910	17.89	11	31836
R20_910_02	910	17.17	11	29921
R20_910_03	910	17.14	11	117900
R20_820_01	820	16.61	13	171949
R20_820_02	820	16.07	10	2293105
R20_820_03	820	16.00	10	94814
R20_820_04	820	15.94	13	44523

R20_760_01	760	15.00	10	659846
R20_760_02	749	15.00	10	19456
R20_760_03	804	15.00	10	78383
R20_730_01	730	14.56	15	2079007
R20_730_02	717	14.00	10	6615916

Table 7. Fatigue results for the **V20** specimens

Specimen ID	Max. cyclic load [N]	Max. cyclic stress [MPa]	Frequency [Hz]	Cycles to failure
V20_1730_01	1730	35.67	5.6	282
V20_1730_02	1730	34.71	5.6	102
V20_1640_01	1640	33.13	6	553
V20_1640_02	1640	32.69	6	549
V20_1640_03	1640	32.61	6	229
V20_1640_04	1640	32.56	6	26
V20_1450_01	1450	29.02	7	1121
V20_1450_02	1450	28.87	7	1635
V20_1450_03	1450	28.71	7	2918
V20_1275_01	1275	25.28	8	3490
V20_1275_02	1275	24.81	8	1692
V20_1275_03	1275	24.73	8	5196
V20_1050_01	1090	20.78	9.2	52801
V20_1050_02	1000	20.51	10	40590
V20_910_01	910	18.03	11	44945
V20_910_02	910	17.80	11	26587
V20_910_03	910	17.67	11	128234
V20_820_01	820	16.94	13	80898
V20_820_02	820	16.63	13	2309037
V20_760_01	760	15.49	10	60877
V20_760_02	760	15.01	10	753688
V20_730_01	730	14.65	15	106296
V20_730_02	730	14.43	15	2096727

Table 8. Fatigue results for the **V90** specimens

Specimen ID	Max. cyclic load [N]	Max. cyclic stress [MPa]	Frequency [Hz]	Cycles to failure
V90_1640_01	1640	34.08	6	92
V90_1640_02	1640	34.07	6	386
V90_1640_03	1640	33.56	6	379
V90_1450_01	1450	29.52	7	642
V90_1450_02	1450	29.26	7	328
V90_1450_03	1450	29.04	7	211
V90_1450_04	1450	27.01	7	268
V90_1275_01	1275	25.52	8	1030
V90_1275_02	1275	25.46	8	1083
V90_1275_03	1275	24.24	8	1625
V90_1275_01	1275	24.94	13.7	2054
V90_1090_01	1090	21.14	9.2	10214
V90_1090_02	1090	20.70	9.2	6872
V90_1090_03	1090	19.30	9.2	21680
V90_910_01	910	19.12	15	28569
V90_910_02	910	17.36	11	9726
V90_910_03	910	17.22	10	64693
V90_820_01	820	17.01	13	103365
V90_820_02	820	16.81	13	264213
V90_730_01	730	15.00	10	141991
V90_730_02	730	14.99	10	375863
V90_730_03	730	13.35	10	711547

V90_730_04	730	12.71	15	2221311
V90_550_01	550	10.76	15	4022702

Table 9. Results from residual strength experiments

Specimen ID	Stiffness [MPa]	Strength [MPa]	Failure strain (%)
Ref_635_02	4720	37.62	0.90
R20_820_02	4495	38.35	0.95
R20_730_01	4169	37.18	1.04
R20_730_02	4258	34.23	0.90
V20_820_02	4483	42.73	1.12
V20_730_02	4451	42.52	1.12
V90_730_04	4866	37.14	0.85
V90_550_01	4618	44.46	1.16

Comparison of the residual strength results to those obtained after the quasi-static experiments shown no significant strength reduction due to the accumulation of the loading cycles. The average residual strength of all run out specimens equals 39.28 MPa, while the average tensile strength for all series equals 39.97 MPa with similar coefficients of variation for both data sets. Nevertheless, the average stiffness of the run out specimens, 4508 ± 229 , was slightly higher than the average quasi-static stiffness of all specimen series, 4245 ± 250 MPa. This stiffening was also observed for some of the specimens failed due to fatigue loading at low stress levels as described in the following. Due to this stiffening, the strain at failure of the run out specimens was slightly lower than the strain at failure measured under the quasi-static experiments.

Fatigue data analysis

All experimental results are plotted in Figs 9-12 and exponential S-N curves are fitted by linear regression as recommended in ASTM E739-10 [56] on the $\text{Log}N$ - σ_{\max} plane. The statistical analysis proposed in [56] assumes that all fatigue data pertain to a random sample (all N data are independent variables), there are neither run-outs nor suspended test data in the dataset, the S-N is described by a linear model ($Y=A+BX$), and a two-parameter log-normal distribution with a constant variable can be used to describe the fatigue life, N . The semi-logarithmic S-N curve equation, shown in Eq. (2) was selected for the statistical analysis of the fatigue data, and the regression analysis results are presented in Table 10. The *CCfatigue* software [57] was used for the estimation of the model parameters for the four examined data sets.

$$\sigma_{\max} = A + B \text{Log}N \quad (2)$$

with σ_{\max} corresponding to the maximum cyclic stress, and N to the number of cycles to failure. It is observed that although all specimen series resulted in similar S-N curves with comparable slopes, those undergone degassing during the manufacturing exhibited less scatter (the variance of the lognormal distribution is clearly lower for **V20** and **V90** specimens – see also Figs 9-12).

Table 10. Regression analysis parameters

	Ref	R20	V20	V90
<i>A</i>	41.87	48.07	47.48	44.98
<i>B</i>	5.59	6.46	6.02	5.85
<i>Variance</i> ($\hat{\sigma}^2$)	0.822	0.825	0.434	0.477

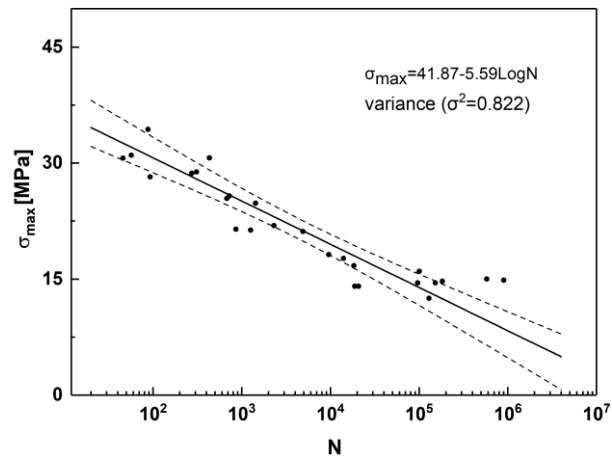


Figure 9. S-N curve for the **Ref** specimen series

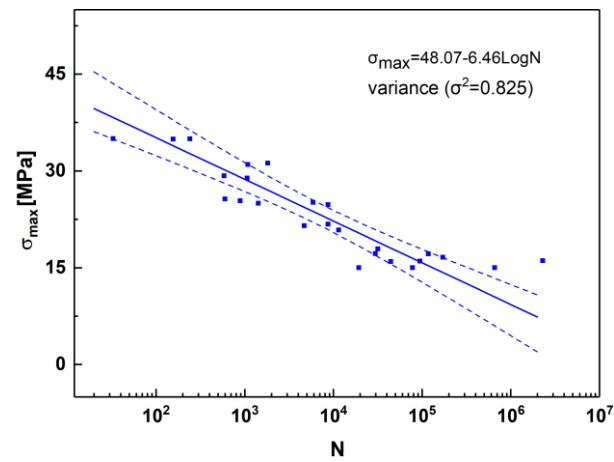


Figure 10. S-N curve for the **R20** specimen series

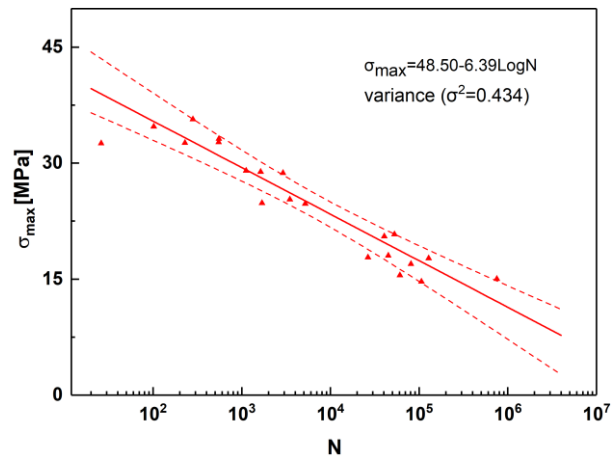


Figure 11. S-N curve for the **V20** specimen series

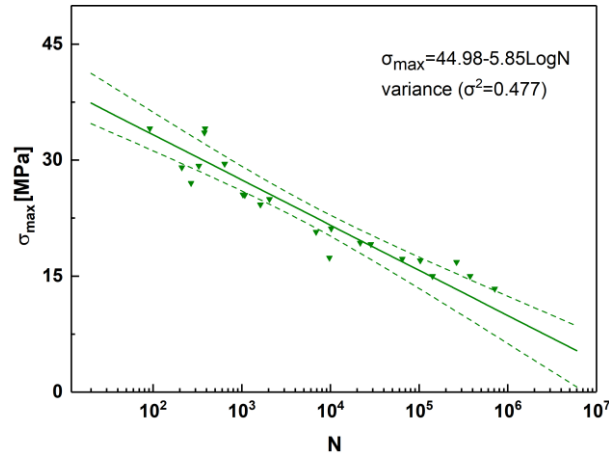


Figure 12. S-N curve for the **V90** specimen series

A comparison of all specimen series' fatigue behavior is performed in the following by using the wear-out model [45, 58]. This model was selected in order to allow the implementation of the quasi-static, as well as the residual strength data obtained by run-out specimens, in the statistical analysis. The wear-out model assumes that the stronger specimen in fatigue should also be the stronger one under quasi-static loads and that therefore a relationship exists between the equivalent static strengths and cyclic stresses and number of cycles to failure. This relationship can be expressed mathematically by the following deterministic equation [58]:

$$\sigma_e = \sigma_{\max} \left[\left(\sigma_r / \sigma_{\max} \right)^{\frac{1}{S}} + (N-1)C \right]^S \quad (3)$$

where σ_e is the equivalent static strength, σ_r , is the residual static strength, N is the number of cycles and S and C are the fatigue model parameters to be determined.

The initial values of S and C should be selected based on available fatigue data with S being the slope of the S-N curve and C a constant defining the shape of the S-N curve for a low-cycle fatigue region. By using the selected S and C values, all data is converted into equivalent static strengths, σ_e , using Eq. (3). A Weibull distribution is then fitted to the equivalent static strength data by using maximum likelihood estimators:

$$P(\sigma_e) = \exp \left[- \left(\frac{\sigma_e}{\beta} \right)^{\alpha_f} \right] \quad (4)$$

This process is performed iteratively for different values of S and C , until the maximum value of the shape parameter, α_f , is obtained [45].

The comparison between the experimental data (with symbols) and the theoretical cumulative distribution (solid lines) of the equivalent static strength data based on the estimated parameters of the Weibull distribution is presented in Figs. 13-14 for all data sets. All data sets are fitted well by the Weibull distribution with those from degassed specimens showing lower variance. Application of a K-S goodness of fit test shown that fitted distributions for all specimen series are accepted at a significance level of 5%.

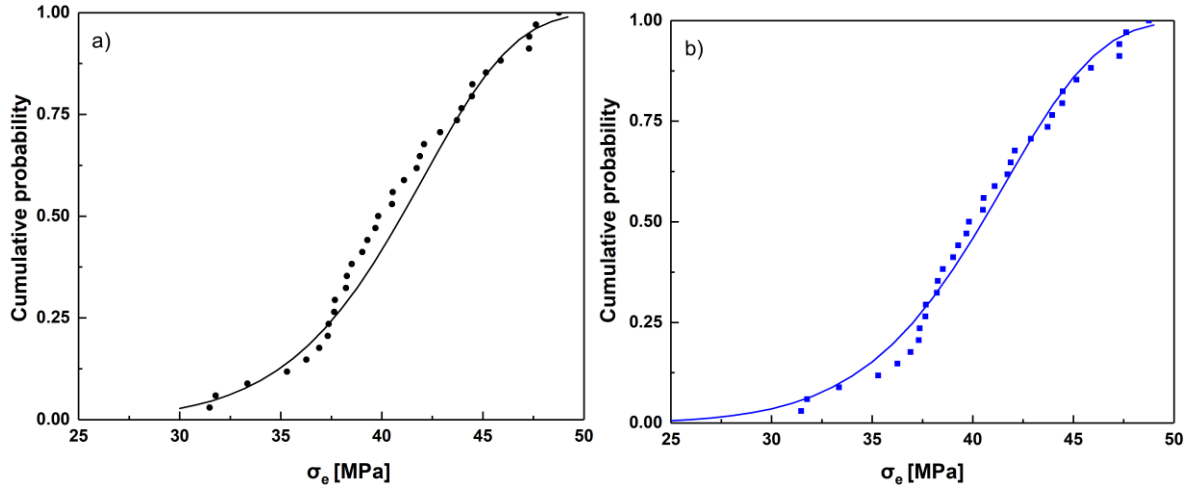


Figure 13. Cumulative probability of the equivalent strength data for (a) **Ref** and (b) **R20** specimen series – Solid line – theoretical values, symbols – experimental data

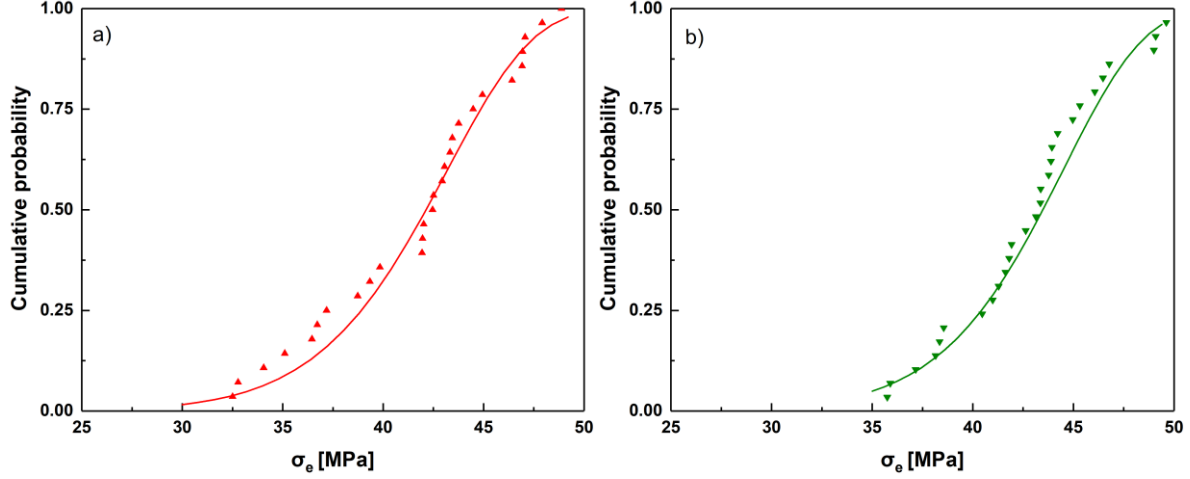


Figure 14. Cumulative probability of the equivalent strength data for (a) **V20** and (b) **V90** specimen series – Solid line – theoretical values, symbols – experimental data

Using the selected/estimated set of parameters S, C, β, α_f , the fatigue curve can be plotted for any desired Sreliability level $P(N)$ (including 50%, representing the mean experimental S-N curve) by using the following equation [45, 58]:

$$\sigma_{\max} = \beta \left\{ \left[-\ln(P(N)) \right]^{\frac{1}{\alpha_f}} \right\} [(N - A)C]^{-S} \quad (5)$$

with $A = (C-1)/C$.

Eq. (5) is a commonly used formulation for the derivation of statistically based S-N curves for composite materials, as explicitly described in [45, 46, 58]. As shown in Fig. 15 the behavior of all sets of specimens can be adequately simulated by power law S-N curve equations. The estimated model parameters are tabulated in Table 11, together with the average UTS of each set at 550 mm/min. Derived S-N curves for all specimen series have typical slopes, similar to those exhibited by other adhesives, [35, 40, 41], composite laminates [48] and adhesively-bonded joints [30]. As expected, the **Ref** specimens are more susceptible to failure at all life regimes. Nevertheless, the S-N curve corresponding to the **V90** specimens exhibits higher slope (S) than all other S-N curves indicating that for high cycle fatigue the **V90** specimens would fail at lower cyclic stresses than any other specimen. The expected inferior fatigue strength of the **Ref** specimens shows that the fatigue response is driven by the strength

and not the elastic properties of the material. All derived S-N curves indicate that the maximum cyclic stress that all material sets can sustain for ca. 2 million cycles (typical for a bridge lifetime) is above 10 MPa.

Table 11. Estimated wear-out model parameters

	Ref	R20	V20	V90
α_f	10.118	9.904	11.586	11.571
β	42.564	42.444	43.906	45.027
S	0.091	0.086	0.085	0.104
C	0.374	0.097	0.111	0.111
UTS [MPa]	40.1	41.6	41.8	39.7

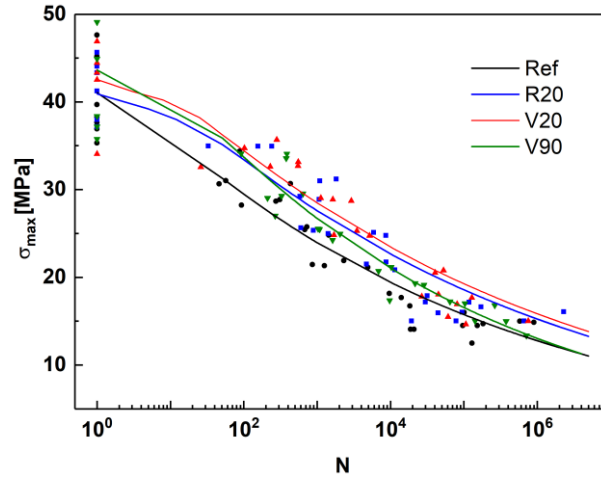


Figure 15. Comparison of all S-N curves derived by the wear-out model

The comparison shown that, the **V20** specimens have the best fatigue performance, being able to sustain longer fatigue life from all other specimen series for the same stress level. The S-N curve corresponding to the **V20** specimens has the smallest slope. Among the other series, the **V90** does not perform well in fatigue, especially at low stress levels where the **V90** specimens fail earlier than those from the **R20** and the **V20** series. **R20** behaves better at high-stress level, which can be linked to the higher strength as shown in Figure 4. On the other hand, the degassed material behaves better at low-stress levels, which can be linked to the reducing of flaws due to the preparation method.

Hysteresis loop areas – fatigue stiffness

The hysteresis area is a measure of the total dissipated energy per cycle; the slope of each stress-strain hysteresis loop corresponds to the fatigue stiffness. If the material shows an elastic behavior and there are no losses due to hysteretic heating, then it can be assumed that the elastic energy equals the total dissipated energy. During a load-controlled fatigue experiment, the hysteresis loops can shift, indicating the presence of creep and the evolution of the average strain per cycle can be monitored to describe creep behavior [35, 48].

Approximately twenty-five load and displacement measurements were recorded per cycle to estimate the stiffness fluctuations and hysteresis loops throughout the fatigue life of all the examined specimens. The applied fatigue loading patterns induced cyclic stresses in the elastic region, while the maximum cyclic strains reached at failure due to fatigue loading increased with increasing stress level; however, they remained below the strains to failure under quasi-static loading at any displacement rate, as shown in Fig. 16. The maximum cyclic strain at failure for the degassed specimens (**V20** and **V90**) is lower from that of the non-degassed ones.

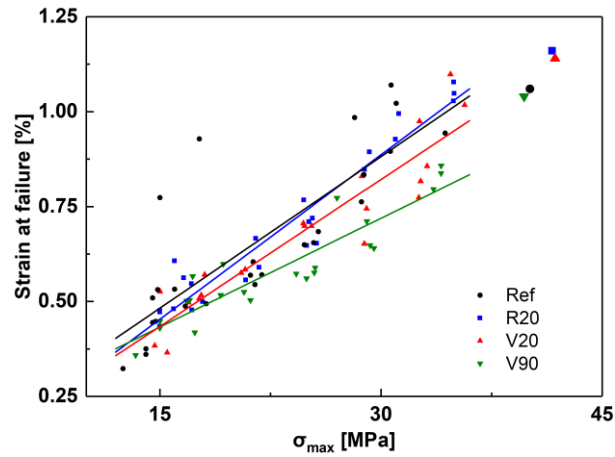


Figure 16. Maximum cyclic strain at failure per stress level, compared to the strain to failure at 550 mm/min (bigger symbols).

Typical hysteresis loops up to failure are presented in Fig. 17 for the **Ref** material series and Fig. 18 for the **V90** material series for both high and low maximum cyclic stresses. At least 20 points were collected during loading for the derivation of each hysteresis loop. The hysteresis area as well as the fatigue stiffness and cyclic creep of all material series did not exhibit significant changes with fatigue cycles for both high and low cyclic stresses. Although only selected results are presented, they are representative of the behavior exhibited by all other specimens. For all specimen series and at all stress levels, the material response shown elastic stress-strain hysteresis loops with little hysteresis area and little stiffness changes, either stiffening or softening as discussed later on.

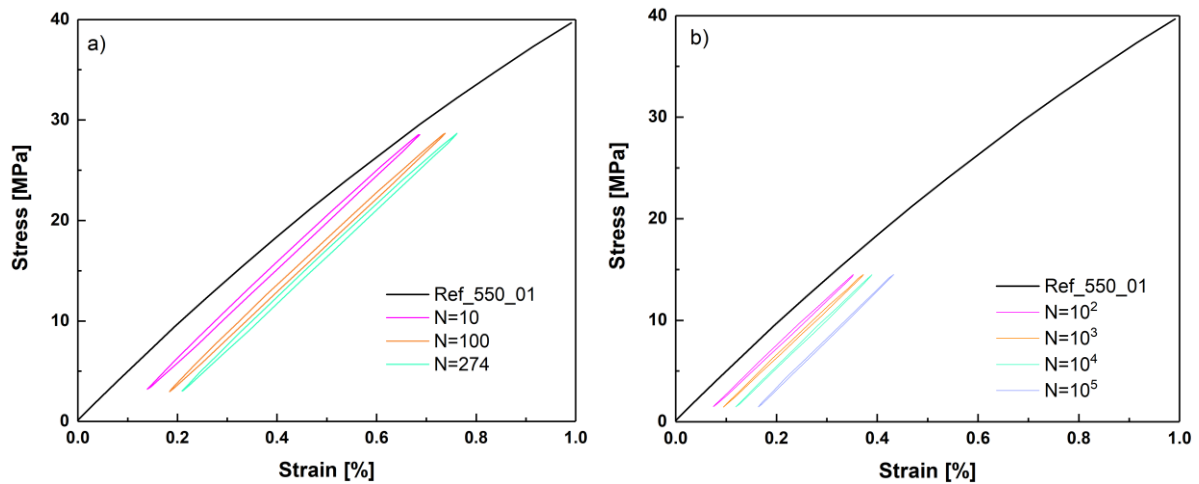


Figure 17. Hysteresis loops for **Ref** specimens a) Ref_1450_02, b) Ref_720_02

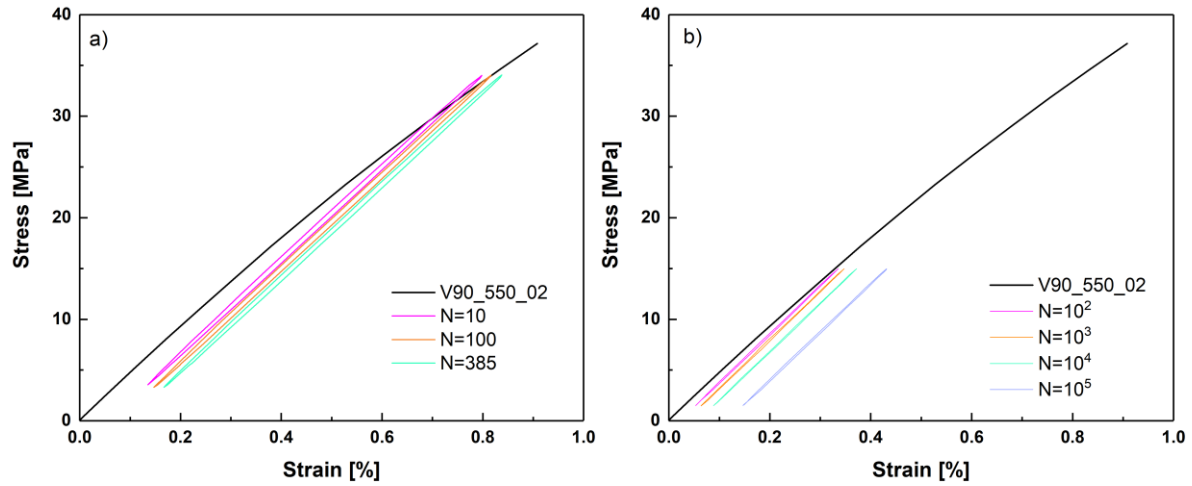


Figure 18. Hysteresis loops for **V90** specimens a) V90_1450_02, b) V90_720_02

Fatigue stiffness was calculated by a linear interpolation of the hysteresis loops at certain numbers of cycles. The stiffness evolution of a selection of specimens from all series is presented in Fig. 19, while a comparison of the stiffness development of specimens of the same series, at different stress levels is shown in Fig. 20. The stiffness of the first hysteresis loop was used for the normalization shown in Fig. 20. The results are presented versus the normalized number of cycles for comparison. Stiffness evolution of the examined specimen series shown different trends. At high stress levels the trend was similar to that observed usually in composites laminates [46] (e.g. specimen V90_1450_01 in Fig. 19 and V20_1275_03 in Fig. 20) with a monotonic decreasing trend until failure. Nevertheless, any stiffness decrease was very little in the range of less than 1% of the initial stiffness. A large number of specimens did not exhibit any measureable stiffness change during the fatigue loading, such as the specimen R20_1800_02 in Fig. 19 or the specimen V20_1050_02 in Fig. 20.

For all specimen series, at lower stress levels, the stiffness was increasing during loading, reaching around 4-5% higher values than the initial, see e.g. specimen Ref_720_02 in Fig. 19 and specimen V20_760_02 in Fig. 20.

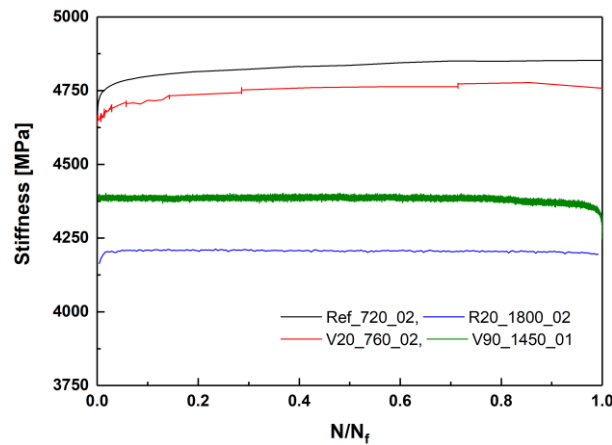


Figure 19. Stiffness evolution trends for specimens from all series

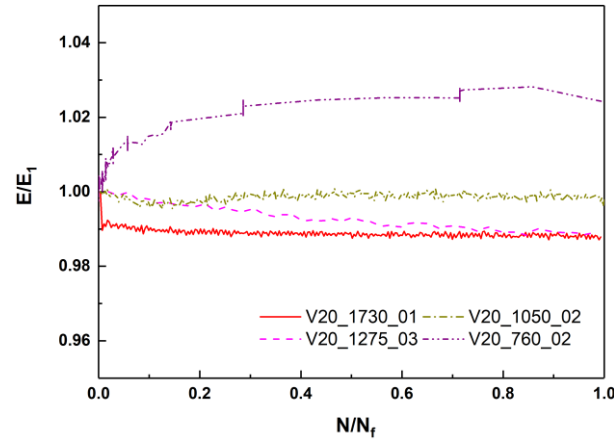


Figure 20. Stiffness evolution for selected **V20** series specimens

This phenomenon was also observed before, [35, 52, 59-61] however, there is no clear explanation for the reason causing this behavior, especially for bulk polymers. In fiber reinforced polymer composites [52, 59] the stiffness increase was attributed to the realignment of the fibers. For bulk polymer adhesives, this behavior was attributed to a molecular realignment of the long chains of polymer molecules leading, under sub-critical stresses, to a better stress redistribution in the material [35, 60]. Nevertheless, although an increase of around 10-15% was observed during fatigue loading of structural adhesives in edge crack torsion (ECT) tests on joints, no explanation was given in [61]. The frequency was low, 0.25Hz, and probably cyclic creep affected this behavior, although not supported by the data. In this work, stiffness increase of around 7% has been also observed during the residual strength experiments performed for all the run out specimens as shown in Table 9. These specimens undergone a large number of low stress cycles before the interruption of the test. Nevertheless, there is no study focusing on the evaluation of the fatigue stiffness, and the analysis of the stiffness increase despite the damage due to fatigue loading.

In addition to the dissipated energy and the fatigue stiffness, the cyclic creep strain can be derived by monitoring the average strain evolution of each hysteresis loop with the number of cycles [35, 48]. Cyclic creep strain is progressively accumulated under stress-controlled cyclic loading of polymer composites [50, 62, 63], as well as of epoxy polymers [39, 64]. This strain is of a viscoelastic nature, as can be confirmed by its complete recovery after load removal [64]. The amount of the accumulated strain depends on the applied cyclic mean stress [39].

The creep strain, i.e., the average cyclic strain, ϵ_{av} , with cycles, increases for all specimens, however at different rates as shown in Fig. 21.

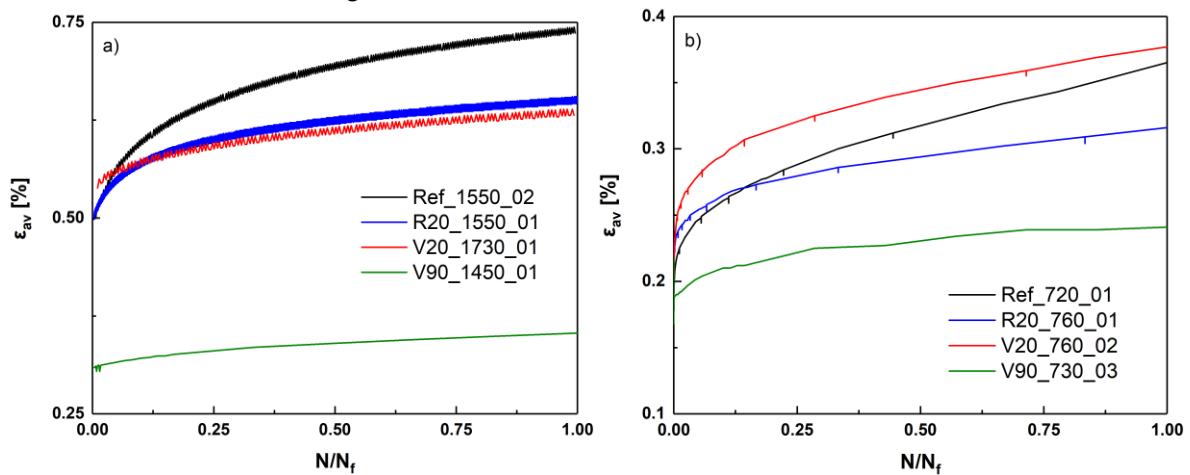


Figure 21. Creep evolution for selected specimens from all series a) high stress levels b) low stress levels

The drifting of the hysteresis loops is more evident for the **Ref**, **R20** and **V20** specimens, while it is less for the **V90** series sets as shown in Fig. 21. The degassing procedure does not seem to affect the cyclic creep strain, nevertheless, as was shown above, due to the immediate hot curing, the **V90** specimens are stiffer than all other series, and therefore show less cyclic creep during fatigue loading at any stress level. The rate decreases with the increasing number of cycles and an asymptotic value of the creep strain is reached for all specimen series at high stress levels (Fig 21a) while a continuous increasing trend is observed for most specimens at lower stress levels. However, in both cases, this phenomenon is reversible; when the cyclic loads are removed, the specimens are able to attain the same tensile (residual) strength in the range of the quasi-static strength. The same behavior, proving the viscoelastic nature of the cyclic creep strain, has been noted in other publications [39, 64, 65, 66] where it was observed that the creep strain, attributed to plasticization, could be fully recovered after load removal [64].

DIC was used in selected fatigue experiments for measuring the surface strain field and allow the estimation of the cyclic Poisson's ratio. Periodical measurements were performed in order to keep a reasonable number of data. The Poisson's ratio was derived by a linear regression of the longitudinal versus the transverse cyclic stress. An example is presented in Fig. 22 using strain measurements recorded between cycles 149 at 151 of the specimen V90_1450_03. The longitudinal and transverse cyclic strains, shown in Fig 22a show a 90° phase. The Poisson's ratio, the slope of the scatter data shown in Fig. 22b, is consistent throughout the fatigue loading, showing slight differences for some of the examined specimens with little scatter, mainly for specimens undergone longer lifetimes. All measured Poisson's ratios are given in Table 12, showing similar values to those derived from the quasi-static experiments.

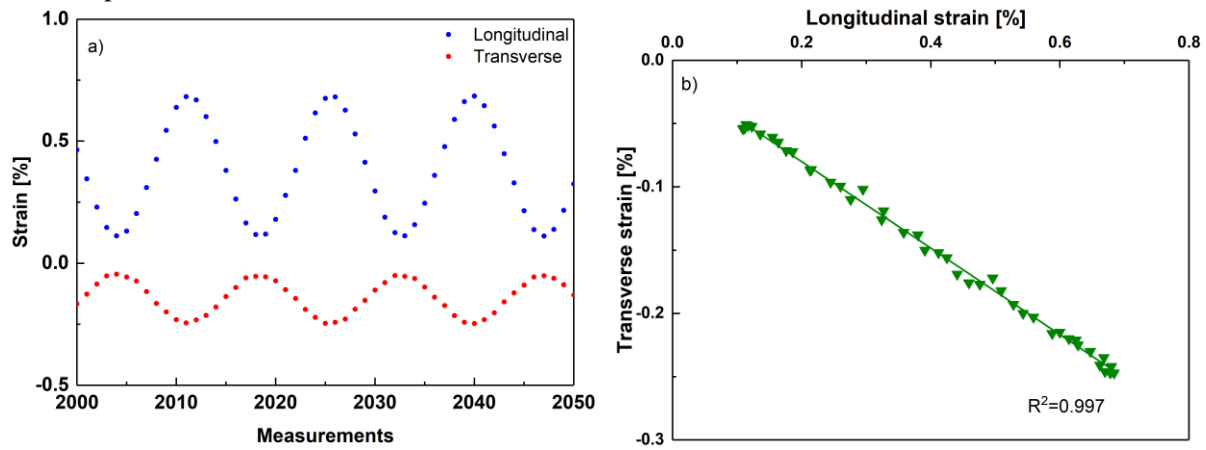


Figure 22: Cyclic Poisson's ratio measurements (V90_1450_03)

Table 12. Cyclic Poisson's ratio

Specimen ID	Frequency [Hz]	Poisson's ratio
Ref_745_01	10	0.391
R20_820_03	10	0.309
R20_760_03	10	0.280
V20_1640_02	6	0.326
V20_910_03	11	0.299
V90_1450_03	7	0.347
V90_820_01	13	0.373
V90_730_01	10	0.289
V90_730_02	10	0.260

Fatigue failure

Failure surfaces of specimens from all series confirm the observation from those of the quasi-static loading. Many small voids can be observed in the volume of the non-degassed specimens, while less

small voids are visible for the degassed specimens. Fatigue loading caused different failure surfaces depending on the stress level as shown in Fig. 23-26 for specimens from all series loaded at high, medium and low stress levels.

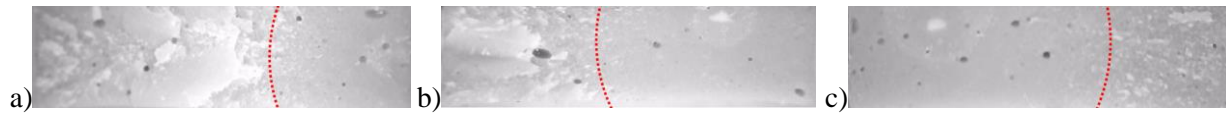


Figure 23. Representative failure surface for a) Ref_1550_02 (N=434), b) Ref_1090_01 (N=2314) c) Ref_730_01 (N=900000)



Figure 24. Representative failure surface for a) R20_1800_03 (N=156), b) R20_1275_03 (N=5926), c) R20_760_01 (N=659846)

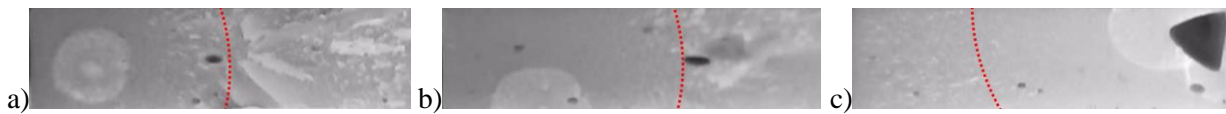


Figure 25. Representative failure surface for a) V20_1640_03 (N=229), b) V20_1275_03 (N=5196) c) V20_730_01 (N=106296)

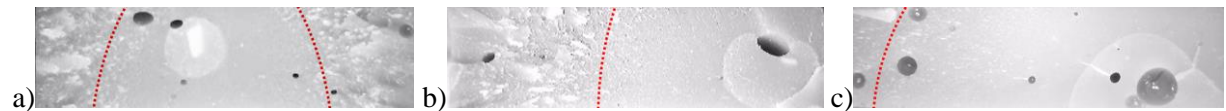


Figure 26. Representative failure surface for V90_1450_02 (N=328), b) V90_1090_01 (N=10214), c) V90_730_03 (N=711547)

At high stress level, the typology of the failure is similar to the one observed for quasi-static tests with an important "teared apart" zone. For lower stress levels however, the fracture tends to be "cleaner" as shown in Figs 23-26 c). In all cases, the failure seems to initiate around an existing defect, either a void (see e.g. Figs. 25b, 25c, 26b)) or a particle inclusion found in the resin volume as shown e.g. in Fig. 24a, 26a. The failure analysis shown that the aforementioned particle inclusions are more frequent in the **V20** series specimens, while specimens from the other series shown a major fraction of void originated critical flaws. This observation indicates that although the degassing reduces the porosity, the hot curing immediately after the casting of the material increases the size of the entrapped voids. There is no evidence that the entrapped voids, although in certain cases were significantly big, affected the material's fatigue performance. Two V20 specimens, both with big voids, loaded at the same stress level, but sustained extremely different numbers of cycles until failure are presented in Fig. 27. While the first specimen failed after ca. 100000 cycles, the second one run out after more than 2 million cycles. Direct comparison of the other characteristics of the failure surface cannot be performed since the second specimen has been fractured during the residual strength experiment.

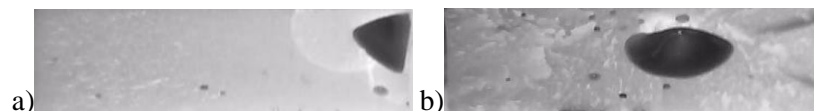


Figure 27. Failure surface of two V20 specs at the same stress level. a) V20_730_01 (N=106296), b) V20_730_02 (N=2096727)

4. Conclusions

An extensive experimental program has been carried to investigate the influence of the preparation and curing conditions on the fatigue behavior of a commercial cold-curing structural adhesive. The

investigation included more than 170 valid quasi-static and fatigue experiments for four types of specimens, each one prepared under different conditions. The following conclusions were drawn from this investigation:

- The examined structural adhesive, independent of the preparation conditions, is capable of attaining fatigue lives of more than 2 million cycles without failure at maximum cyclic stress levels of higher than 10 MPa.
- Degassing during fabrication improved the specimen quality and decreased the scatter of the results. Especially the degassing process without additional heating after casting (**V20**) improved the material quality, reducing the entrapped air voids. **V20** specimens shown increased stiffness and tensile strength as well as better fatigue performance than all other specimen series. Post-curing improved the material performance, however the immediate post curing performed for the **V90** specimens led to inferior fatigue properties for this material series, especially at the high cycle fatigue region.
- The examined sets of specimens showed a fatigue behavior similar to that presented in previous works for bulk epoxy adhesives, but also for fiber-reinforced composite materials, with smooth power law S-N curves with slopes around 10. The steeper S-N curve corresponds to the **V90** specimens, while the three other curves derived from the fatigue results of the **Ref**, the **R20** and the **V20** specimens had the same slope. The **V90** specimens, although proved more susceptible to fatigue loading especially at low stresses, exhibited more consistent fatigue behavior, with less scatter estimated for their fatigue results.
- Hysteresis loop area did not show any significant changes with loading cycles for all specimen series. Stiffness increase was observed for low stress level fatigue experiments, but also after the residual strength tests. No evidence for the reasons causing this phenomenon can be derived from this work. For higher stress-level, the stiffness remained constant or slightly decreased during the cyclical loading.
- Negligible temperature increase was measured for all specimens and frequencies up to 15 Hz. As the ASTM D7791 suggests frequencies up to 25 Hz. Nevertheless, in this work, with increasing frequency more tab failures occurred.
- A method of monitoring the fatigue testing via DIC was tested with encouraging results. DIC was successfully used in this work to measure Poisson's ratio both in quasi-static and in fatigue loading.
- A clear strain-rate effect was observed for all specimens. Performance of quasi-static experiments at loading rates similar to those of the fatigue loading is crucial, when it is intended to mix both data sets for any further analysis.

Acknowledgements: The authors acknowledge the assistance provided by the technical team of the structural engineering Experimental platform (GIC-ENAC at the Ecole Polytechnique Fédérale de Lausanne (EPFL), Switzerland) for the use of testing equipment, and the support of Sika AG, Zurich that provided the epoxy material. The second author wishes also to acknowledge the grant SFRH/BSAB/150266/2019, provided by Fundação para a Ciência e a Tecnologia, IP (FCT), financed by European Social Fund and by national funds through the FCT/MCTES.

5. References

1. Kinloch AJ. Adhesion and adhesives: science and technology. Springer-Science+Business Media,B.V. 1987.
2. Mays GC, Hutchinson AR. Adhesives in civil engineering. Cambridge University Press. 1992.
3. Sims FA. Applications of resins in bridge and structural engineering. *International Journal of Cement Composites and Lightweight Concrete* 1985; 7:225-32.
4. Michels J, Sena-Cruz J, Czaderski C, Motavalli M. Structural strengthening with prestressed CFRP strips with gradient anchorage. *Journal of Composites for Construction* 2013; 17:651-661.

5. Kumar P, Patnaik A, Chaudhary S. A review on application of structural adhesives in concrete and steel-concrete composite and factors influencing the performance of composite connections. *International Journal of Adhesion and Adhesives* 77 (2017) 1-14.
6. Keller T, Rothe J, de Casto J, Osei-Antwi M. GFRP-Balsa Sandwich Bridge Deck: Concept, Design, and Experimental Validation. *J. Compos., Constr.* 2014, 18(2): 04013043.
7. Reising RMW, Sharooz BM, Hunt VJ, Neumann AR, Helmicki AJ, Hastak M. Close Look at Construction Issues and Performance of Four Fiber-Reinforced Polymer Composite Bridge Decks. *J. Compos. Constr.*, 2004, 8(1): 33-42.
8. EN 1991-2 Eurocode 1. Actions on structures – Part 2: Traffic loads on bridge. European committee for standardization. 2003.
9. Zarouchas D, Nijssen. Mechanical behaviour of thick structural adhesives in wind turbines blades under multi-axial loading. *Journal of Adhesion Science and Technology*, 2016, 30:13,1413-1429.
10. Fatigue Life Prediction of Composites and Composite Structures – Second Edition, A. P. Vassilopoulos (Ed.) Woodhead Publishing, 2019
11. Moussa, O., Vassilopoulos, A.P., Castro, J.D., Keller, T. Long-term development of thermophysical and mechanical properties of cold-curing structural adhesives due to post-curing. *J Appl Polym Sci*, 2013;127(4):2490-2496
12. Moussa, O., Vassilopoulos, A.P., Castro, J.D., Keller, T. Early-age tensile properties of structural epoxy adhesives subjected to low-temperature curing. *Int J Adhes Adhes*, 2012;35:9-16
13. Hutchinson AR. Durability of structural adhesive joints. PhD thesis. University of Dundee, 1986.
14. Moussa O. Thermophysical and Thermomechanical Behavior of Cold-Curing Structural Adhesives in Bridge Construction. PhD #5244. EPFL. 2011.
15. Carbas RJC, Marques EAS, Da Silva LFM, Lopes AM. Effect of Cure Temperature on the Glass Transition Temperature and Mechanical Properties of Epoxy Adhesives. *The Journal of Adhesion*. 2014. 90:104-119.
16. Wu C-S. Influence of post-curing and temperature effects on bulk density, glass transition and stress-strain behaviour of imidazole-cured epoxy network. *Journal of Materials Science*. 27(1992): 2952-2959.
17. Sancaktar E. The effects of cure temperature and time on the bulk tensile properties of a structural adhesive. *J Adhesion*, 1983;15:241-264.
18. Carbas RJC, da Silva LFM, Marques EAS, Lopes AM. Effect of post-cure on the glass transition temperature and mechanical properties of epoxy adhesives. *Journal of Adhesion Science and Technology*, 2013;27(23):2542-2557
19. Broutman LJ, Gaggar SK. Fatigue behavior of epoxy and polyester resins. *Int J Polym Mater Po* 1972; 1(1972): 295-316.
20. Product Data Sheet. Sikadur®-330. May 2017, Version 02.01.
21. De Castro J, Keller T. Ductile double-lap joints from brittle GFRP laminates and ductile adhesives. Part I: Experimental investigation. *Compos Part B-Eng*, 2008; 39(2): 271-281.
22. Michels J, Sena Cruz J, Christen R, Czaderski C, Motavalli M. Mechanical performance of cold-curing epoxy adhesives after different mixing and curing procedures. *Composites Part B* 2016;98:434-443.
23. Katnam KB, Stevenson JPI, Stanley WF, Buggy M, Young TM. Tensile strength of two-part epoxy paste adhesives: Influence of mixing technique and micro-void formation. *International Journal of Adhesion & Adhesives* 31 (2011): 666-673.
24. Sánchez Cebrián A, Zogg M, Ermanni P. Methodology for optimization of the curing cycle of paste adhesives. *International Journal of Adhesion & Adhesives* 2013;40:112-119
25. Angelidi M, Vassilopoulos AP, Keller T. Displacement rate and structural effects on Poisson ratio of a ductile structural adhesive in tension and compression. *International Journal of Adhesion and Adhesives*. 78 (2017) 13-22.
26. Kanchanomai C, Rattananon S, Soni M. Effects of loading rate on fracture behavior and mechanism of thermoset epoxy resin. *Polymer Testing* (24); 2005: 886-892.

27. Banea MD, de Sousa FSM, da Silva LFM, Campilho RDSG, Bastos de Pereira AM. Effects of Temperature and Loading Rate on the Mechanical Properties of a High Temperature Epoxy Adhesive. *Journal of Adhesion Science and Technology*. Vol. 25 (8); 2011: 2461-2474.
28. Zhang M, Jiang B, Chen C, Drummer D, Zhai Z. The effect of temperature and strain rate on the interfacial behavior of glass fiber reinforced polypropylene composites: A molecular dynamics study. *Polymers* 2019, 11, 1766.
29. Sarfaraz, A. P. Vassilopoulos, T. Keller. "Experimental investigation of the fatigue behavior of adhesively-bonded pultruded GFRP joints under different load ratios" *Int J Fatigue*, 2011;33(11):1451-1460
30. Sarfaraz R, Vassilopoulos AP, Keller T. Experimental investigation and modeling of mean load effect on fatigue behavior of adhesively-bonded pultruded GFRP joints. *International Journal of Fatigue* 44, 2012: 245-252.
31. Y. Zhang, A. P. Vassilopoulos, T. Keller. "Fracture of adhesively-bonded pultruded GFRP joints under constant amplitude fatigue loading" *Int J Fatigue*, 2010;32(7):979-987
32. M. Shahverdi, A. P. Vassilopoulos, T. Keller. "A total fatigue life model for the prediction of the R-ratio effects on fatigue crack growth of adhesively-bonded pultruded GFRP DCB joints" *Compos A: Appl Sci and Manufacturing*, 2012;43(10):1783-1790
33. Abdel Wahab MM. Fatigue in Adhesively Bonded Joints: A Review. *ISRN Materials Science*, 2012;746308.
34. Bernasconi, A., Beretta, S., Moroni, F., Pirondi, A. Local stress analysis of the fatigue behaviour of adhesively bonded thick composite laminates" *J Adhesion*, 2010;86(5-6):480-500
35. Savvilitidou M, Keller T, Vassilopoulos AP. Fatigue performance of a cold-curing structural epoxy adhesive subjected to moist environments. *International Journal of Fatigue* 103 (2017): 405-414.
36. M. Rosemeier, A. Krimmer, A. Bardenhagen, A. Antoniou. Tunneling Crack Initiation in Trailing-Edge Bond Lines of Wind-Turbine Blades. *AIAA Journal*, 2019, 57(12):5462-5474
37. Tao G, Xia Z. Biaxial fatigue behavior of an epoxy polymer with mean stress effect. *Int J Fatigue* 2009; 31: 678-685.
38. Tao G, Xia Z. Fatigue behavior of an epoxy polymer subjected to cyclic shear loading. *Mater Sci Eng A* 2008; 486: 38-44.
39. Tao G, Xia Z. Ratcheting behaviour of an epoxy polymer and its effect on fatigue life. *Polym Test* 2007; 26: 451-460.
40. Stammes E, Nijssen RPL, Westphal T. Static and fatigue tests on resin for wind turbine rotor blades. 14th ECCM, Budapest. 2014.
41. G-T Wang, H-Y Liu, N. Saintier, Y-W. Mai. Cyclic fatigue of polymer nanocomposites. *Eng Fracture Analysis*, 2009;16:2635-2645
42. C. M. Manjunatha, A. C. Taylor, A. J. Kinloch, S. Sprenger. The cyclic-fatigue behavior of an epoxy polymer modified with micron-rubber and nano-silica particles. *J Mater Sci* 2009;44:4487-4490
43. Broutman LJ, Gaggard SK. Fatigue behavior of epoxy and polyester resins. *Int J Polym Mater Po* 1972; 1(1972): 295-316.
44. He X. Effect of mechanical properties of adhesives on stress distributions in structural bonded joints. *Proceedings of the world congress on engineering 2010 vol II*, WCD 2010, June 30-July 2, 2010, London.
45. R. Sarfaraz, A. P. Vassilopoulos, T. Keller. "Modeling the constant amplitude fatigue behavior of adhesively bonded pultruded GFRP joints" *J Adhes Sci Technol*, 2013;27(8):855-878
46. A. P. Vassilopoulos. "The history of fiber-reinforced polymer composite laminate fatigue" *Int. J. Fatigue*, 2020;134:105512
47. J. Brunbauer, H. Stadler, G. Pinter. "Mechanical properties, fatigue damage and microstructure of carbon/epoxy laminates depending on fibre volume content" *Int J Fatigue*, 2015;70:85-92
48. Movahedi-Rad, A.V., Keller, T., Vassilopoulos, A.P. "Fatigue damage in angle-ply GFRP laminates under tension-tension fatigue" *Int J Fatigue*, 2018;109:60-69

49. Sun CT, Chim ES. Fatigue retardation due to creep in a fibrous composite. *Fatigue of Fibrous Composite Materials*. ASTM International, 1981.
50. T.H. Courtney, J Wulff "Matrix-limited fatigue properties of fibre composite materials" *J Mater Sci* 1966;1:383-388
51. G. C. Shih, L. J. Ebert "The effect of the fiber/matrix interface on the flexural fatigue performance of unidirectional fiberglass composites" *Compos Sci Technol*, 1987;28:137-161
52. Movahedi-Rad, A.V., Keller, T., Vassilopoulos, A.P. "Interrupted tension-tension fatigue behavior of angle-ply GFRP composite laminates" *Int J Fatigue*, 2018;113:377-388
53. ASTM D638-14. Standard test method for tensile properties of plastics. ASTM International, West Conshohocken, PA, 2014.
54. ASTM D7028-07^{e1}. Standard test method for glass transition temperature (DMA T_g) of polymer matrix composites by dynamic mechanical analysis (DMA). ASTM International, West Conshohocken, PA 19428-2959. 2008.
55. ASTM D7791-12. Standard test method for uniaxial fatigue properties of plastics. ASTM International, West Conshohocken, PA 19428-2959. 2012.
56. ASTM E739-10. Standard practice for statistical analysis of linear or linearized stress-life (S-N) and strain-life (ϵ -N) fatigue data. ASTM International, West Conshohocken, PA 19428-2959. 2015.
57. Vassilopoulos AP, Sarfaraz R, Manshadi BD, Keller T. A computational tool for the life prediction of GFRP laminates under irregular complex stress states: Influence of the fatigue failure criterion. *Comp. Mater Sci* 2010; 49: 483-491.
58. Sendeckyj G. Fitting Models to Composite Materials Fatigue Data. *Test Methods and Design Allowables for Fibrous Composites*. STP29314S, C. Chiamis, Ed., ASTM International, West Conshohocken, PA (1981) 245-260.
59. Movahedi-Rad, A.V., Keller, T., Vassilopoulos, A.P. "Creep effects on tension-tension fatigue behavior of angle-ply GFRP composite laminates" *Int J Fatigue*, 2019;123:144-156
60. Takemori MT. Polymer Fatigue. *Ann. Rev. Mater. Sci.* 1984. 14 : 171-204.
61. P. Bidaud. Analysis of the cyclic behavior of an adhesive in an assembly for offshore windmills applications. *Materials*. Université Bretagne Occidentale, 2014.
62. D. Samborsky, J. F. Mandell, D. A. Miller, Creep/Fatigue behavior of resin infused biaxial glass fabric laminates, *AIAA SDM Wind energy Session*, 2013.
63. A. D. Drozdov, Cyclic viscoelastoplasticity and low-cycle fatigue of polymer composites, *Int. J. Solids Struct.* 48 (2011) 2026–2040.
64. X. Shen, Z. Xia, F. Ellyin, Cyclic deformation behavior of an epoxy polymer. Part I: Experimental investigation, *Polym. Eng. Sci.* 44 (2004) 2240–2246.
65. A. Benaarbia, A. Chrysochoos, G. Robert, Thermomechanical behavior of PA6.6 composites subjected to low cycle fatigue, *Compos. Part B Eng.* 76 (2015) 52–64.
66. C. Blanchard, A. Chateauminois, L. Vincent, A new testing methodology for assessment of fatigue properties of structural adhesives, *Int. J. Adhes. Adhes.* 16 (1996) 289–299.